

1 Integrated interpretation of geophysical data from Zagros mountain belt (Iran)

2 Mansoure Montahei*(1), Pilar Queralt (2), Juanjo Ledo (2), Behrooz Oskooi (1), Josep A. Muñoz (2),
3 and Alex Marcuello (2)

4 (1) Institute of Geophysics, University of Tehran, Iran, (2) Institut de Recerca GEOMODELS.

5 Departament de Dinàmica de la Terra i de l'Oceà. Universitat de Barcelona, Barcelona, Spain

6 Abstract

7 Fluid composition and distribution, the key factors determining geoelectric structure in a
8 seismically active region, are controlled by local and regional stresses and rheological contrasts. In
9 the central Zagros collision zone, one of the world's most seismically active mountain belt, almost
10 coincident magnetotelluric and seismic velocity profiles are jointly interpreted to recover more
11 accurately structural boundaries and fluid distribution within the crust.

12 A multi-site and multi-frequency approach was used for the strike analysis of regional structure
13 and decomposition of distortion effects on magnetotelluric data. Distortion corrected
14 magnetotelluric data were then used for two- dimensional inversion modeling. The results image a
15 thick conductive overburden in the southwest of the profile, high conductivities attributed to the
16 fault zone conductors (FZCs) and an almost concave conductor extending from middle to lower
17 crust in the central- eastern portion of the mountain belt, beneath the High Zagros (HZ).

18 Comparison with the already available S- velocity structure, obtained by joint inversion of P-wave
19 receiver functions and surface wave dispersion data, shows that these main conductive features are
20 spatially correlated with a low-velocity layer representative of the sedimentary cover overlying the
21 Arabian platform and a velocity contrast bounded by the main Zagros thrust (MZT) fault, indicating
22 the presence of fault zone fluids. The joint interpretation of magnetotelluric inverse modeling and
23 seismicity data also shed light on fluid generation influencing rock deformation and seismicity in
24 this region. It suggests that beneath the HZ, deep crustal fluids generated through metamorphism
25 may promote aseismic deformations before high stresses are buildup and cause the north- eastern
26 part of the Zagros Fold and Thrust Belt (ZFTB) to be seismically inactive compared to its south-
27 western part.

28 1. Introduction

29 The Zagros orogene is a key structural element of the Alpine-Himalian belt. The range represents
30 the surface exposure of the Arabian-Eurasian collision, known as an example of a young collision
31 system and accommodates spectacular, world-renowned whaleback folds, hosting vast petroleum
32 reserves. It is amongst the most rapidly deforming and seismically active fold and thrust belts and
33 proved to be an ideal setting in which to investigate competing models of fold and thrust

34 deformation (Nissen et al., 2011). Studying deep crustal structure of the Zagros belt could thus
35 provide better understanding of the dynamic earth processes in a continental collision.

36 Most of the structural studies are based on the measurements of surface geology and instrumental
37 earthquake records. Earlier studies suggest that larger earthquakes occurred in the Zagros
38 basement (Talebian_& Jackson 2004). Recent studies of earthquake faulting based on radar
39 interferometry show a depth distribution of coseismic faulting; while the moderate size (5- 6 Mw)
40 earthquakes ruptured the competent group of mechanically strong strata in the lower sedimentary
41 cover (at depths of 5- 10 km), their micro-seismic aftershocks are vertically separated and occurred
42 within the basement at depths of ~ 10- 20 km. Coulomb stress changes, the effects of loading or
43 shaking and dynamic stress transfer caused by shaking are possible scenarios lead to the
44 separation (Nissen et al., 2011).

45 Nevertheless, very few geophysical investigations have been conducted to constrain the deep
46 crustal structure of the Zagros. To improve our knowledge about the crustal structure of Zagros
47 collision zone, we analyze broadband magnetotelluric (MT) data, recorded at 46 stations along a
48 470 Km profile, crossing the main morpho-tectonic units in this region (Figure 1). It starts near
49 Busher on the northern coast of Persian Gulf, crosses the ZFTB, where a high level of seismicity is
50 accommodated with earthquakes magnitudes smaller than 7 and hypocenters concentrated at a
51 depth between 8-15 Km. To the NE the profile further crosses the Precambrian metamorphic rocks
52 of Sanandaj Sirjan Zone (SSZ), bounded by the Urumieh-Dokhtar magmatic assemblages (UDMA)
53 produced by the Eiocen to present time volcanic activities. The profile ends near Yazd, in the SW of
54 central Iran micro-continent (CIMC) block. The data were preliminary interpreted by 2D inverse
55 modeling (Oskooi et al., 2013) and further investigated by sensitivity analysis of the inversion
56 results (Layegh-Haghighi et al., 2018). This paper extends our previous findings by removing
57 distortion effects from MT data to obtain a new and more accurate 2D resistivity model. In the next
58 stage, we jointly interpret inversion results with the recent seismicity data and the latest seismic
59 velocity models (Karasözen et al, 2019; Moteghi et al., 2015). Joint interpretation of seismic velocity
60 and electrical resistivity models allows to better constraint geological scenarios (Gabàs et al., 2016;
61 García-Yeguas et al., 2017)

62

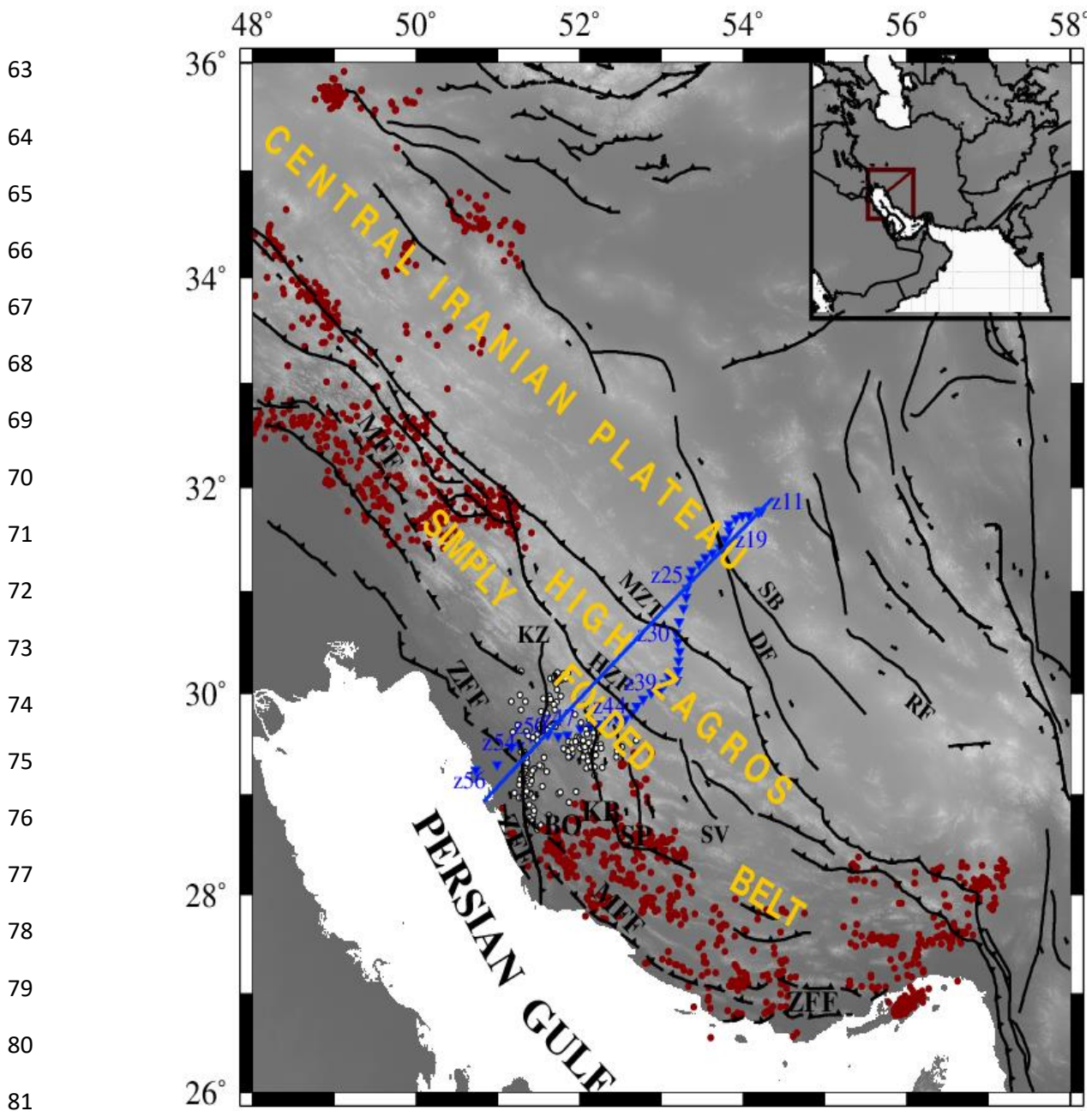


Figure 1. Geological map of the Zagros mountain belt showing the location of MT sites (blue inverse triangles) and the 2-D modeling profile (blue line). Also shown are the main structural units (Simply Folded Belt, High Zagros and Central Iranian Plateau) and the major faults (black lines, dashed if blind): BO, Borazjan Fault; DEF, Dezful Embayment Fault; KZF, Kazerun Fault; MFF, main front fault; HZF, High Zagros Fault; MZT, Main Zagros Thrust Fault; SV, Sarvestan Fault; SP, SabzPushan Fault; SU, Surmeh Fault; ZFF, Zagros Foredeep Fault; DF, Dehshir Fault; SB, Shahr e Babak fault. White and maroon dots are epicentres from GCCEL database (Karasozen et. al., 2019), the white ones are projected in the 2D MT resistivity model. The inset shows the location of the regional map.

2. Geological setting and geophysical background

Subsequent to the closure of the Neothetys ocean and its subduction beneath Iranian microplate during Mesozoic and early Cenozoic, the deformed north-eastern edge of the Arabian plate collided

89 obliquely with central Iran continental block. Zagros mountain belt was formed as the surface
90 exposure of this collision. Magneto-stratigraphy and strontium isotope stratigraphy of the foreland
91 basin sedimentation restricted the initial stage of mountain building at 27 ± 2 Ma (Pirouzet.al.,
92 2017). The estimates of underthrust Arabian lithosphere (≈ 350 Km) and the average shortening
93 rate across the Zagros (ca. 13.5 mm/yr) implied that almost half of the convergence between
94 Arabia and Eurasia is manifested by the crustal thickening across the Zagros and the remained
95 shortening is due to the thrusting and eclogitization of the Arabian crust (Pirouz et al., 2017; Paul et
96 al., 2010; Masson et al, 2005).

97 Based on topography, exposed stratigraphy, and seismicity, the Zagros Fold and Thrust Belt (ZFTB)
98 can be divided by the High Zagros fault (HZF) into two distinct zones: the Simply Folded Belt (SFB)
99 in the southwest and the High Zagros (HZ) in the northeast. While the topography is lower than
100 1500 m throughout the SFB with rare exposes of Paleozoic strata, the topography averages 1500-
101 2000 m and the stratigraphy exposes Paleozoic and Mesozoic levels in the High Zagros (Nissen et
102 al., 2011).

103 While geological complexities make control-source seismic imaging of Moho depth variation
104 impossible, most of our knowledge about crustal and lithospheric upper mantle velocity structure
105 comes from seismology and non-seismic geophysical data (Paul et al., 2010).

106 The first coarse map of MOHO depth variation beneath the Zagros Orogeny, provided by the
107 modeling of the Bouguer anomaly data, showed crustal thickening from 40 km beneath the Persian
108 Gulf to 65 km beneath the MZT (Dehghani and Makris, 1984; Snyder and Barazangi, 1986).
109 However, receiver function analysis of teleseismic earthquake details showed that crustal thickness
110 is 42 ± 2 km beneath the ZFTB. From 30 km SW of the MZT, crustal thickness increases on a 170 km
111 length and reaches a maximum value of 69 ± 2 km beneath the low elevation of SSZ (and not beneath
112 the High Zagros) between 50 and 90 km NE of the MZT. The MOHO depth decreases to its average
113 value around 45 km, beneath CIMC (Paul et al., 2006). These values are consistent with the crustal
114 thicknesses obtained from 1D absolute S-velocity model beneath each station (Motaghi et al., 2015)
115 and also the depth section of S-wave receiver functions (SRFs, Motaghi et al., 2017).

116 Lithosphere is thick beneath the Zagros (thicker than 240 km) and becomes relatively thinner
117 (130 ± 15 km) beneath CIMC (Motaghi et al., (2015)).

118 Upper mantle structure and mantle transition zones, based on the PRF migrated depth section
119 down to 800 km depth (Motaghi et al., 2017), show: (i) an intra lithospheric mantle decoupling,

120 which lets on differential buckling and introduces a deforming viscose layer representative of the
121 lid rheological parameters, ii) lithospheric scale accommodation of the south Zagros contract, (iii)
122 minor thrusting of lithospheric mantle beneath central Iran, indicating that Zagros collision is in its
123 initial stage and (iv) a low dip slab subduction coincident with the slab stagnation close to the
124 transition zone (Manaman et al. 2011).

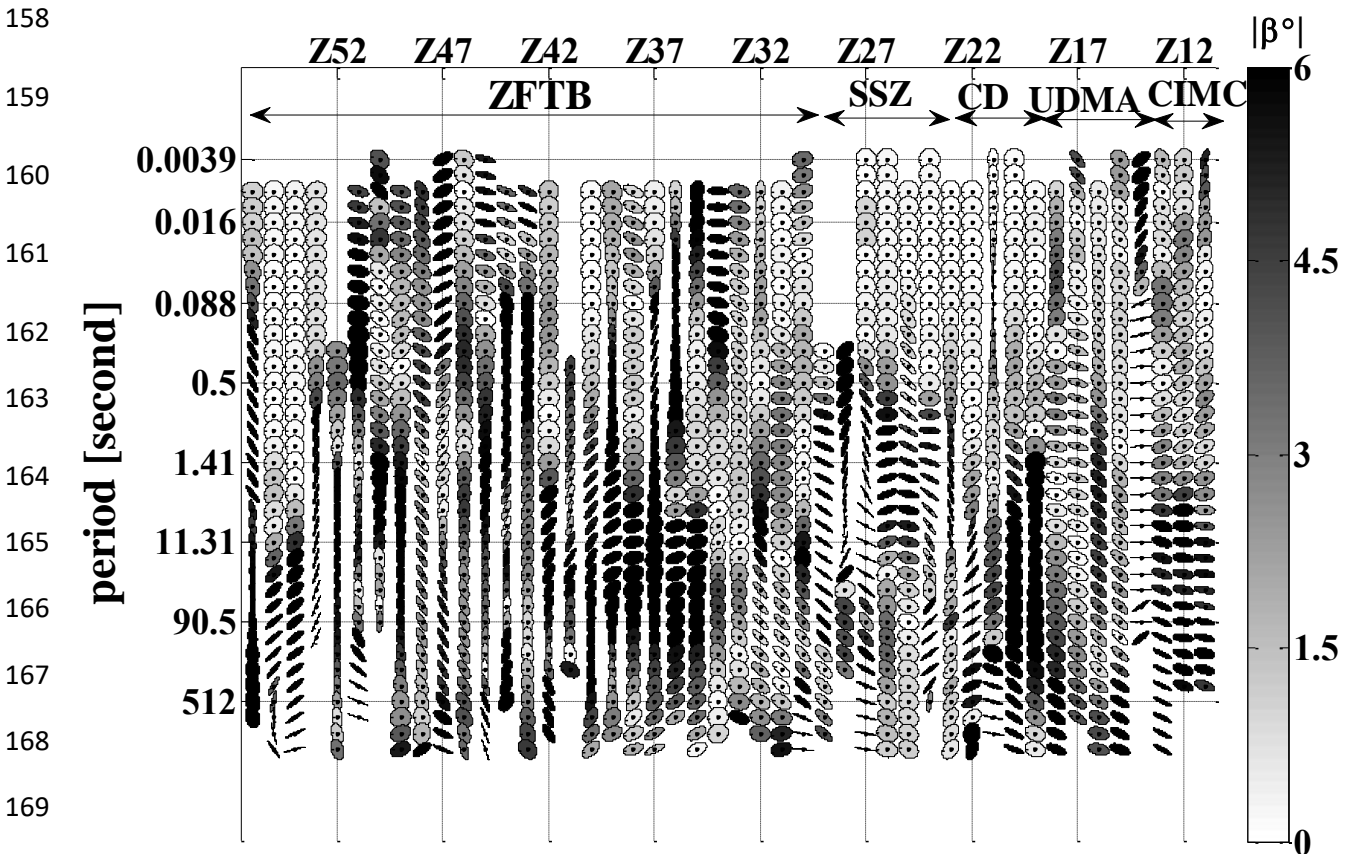
125 There is no basement outcrop in the Zagros, however different estimates of the total sedimentary
126 cover show its thickness varies from ~ 14 km in the northwest of SFB to ~ 10 km in the far
127 southeastern of SFB. To the northeast, into the HZ, it decreases to lower values due to the erosion
128 (Sherkati et al., 2006). Furthermore, a recent inverse modeling of potential field data shows high
129 density contrasts of the embedded units among active faults in this region (BF, KZF, MFF, and HZF
130 faults), which represent basement rocks uplifted close to the surface (Abedi et. al., 2018).

131 **3. Magnetotelluric data Analysis and Inversion**

132 The MT method is a passive electromagnetic exploration technique which records naturally varying
133 horizontal electric and magnetic fields as well as the vertical component of the magnetic field. MT
134 transfer functions are calculated at different frequencies of each station as the ratio of mutually
135 perpendicular electric and magnetic field components in the horizontal plane, termed as impedance
136 tensor elements and also the ratio of horizontal to vertical magnetic field components, known as
137 tipper vectors. The magnitude (scaled as apparent resistivity) and phase of impedance tensor
138 elements are commonly used for MT data presentation. Penetration depths of EM fields depend on
139 their frequencies (increase with decreasing frequency) as well as the electrical conductivity of the
140 subsurface and provide depth sounding estimates of the MT transfer functions. In 2D earth
141 situations, where electrical resistivity is constant along one of the horizontal direction (strike
142 direction of the regional structure) EM fields are decomposed into two distinct modes; transverse
143 electric (TE) and transverse magnetic (TM) modes (Chave and Jones, 2012). The MT method allows
144 unraveling the electrical resistivity of the subsurface at lithospheric scales and define complex
145 structure and tectonic history of collision zones (Unsworth, 2010 and the case studies therein).

146 The phase tensor method (Caldwell et al., 2004) was employed to determine the dimensionality of
147 the data. A map of phase tensor ellipses at the different periods of all sites is presented in figure 2.
148 For most sites at short periods, where EM fields have small penetration depths, they are circles,
149 characteristic of 1D regional geoelectric structure at these depths. Increasing the period,
150 penetration depths get larger and the phase tensors delineate ellipses whose major and minor axes
151 are parallel or perpendicular to the N45°W direction. Considering the 90° ambiguity inherent in the

152 method, this direction is coincident with the general trend of the ZFTB, as the main geologic
 153 structure in this region. Furthermore, the face color of the phase tensors is determined by the β
 154 skew angle, a distortion free measure of asymmetric properties introduced in the data by 3D
 155 structures. The accepted value of this parameter above which the structure could not be considered
 156 as 2D is 5° . The small β skew angles calculated at most periods for all sites implement that a 2D
 157 inverse modeling strategy is acceptable for this data set.



170 Figure2. The phase tensor ellipse map showing the dimensionality for the Zagros profile. The major and minor axes of the
 171 ellipses correspond to the strike direction of regional geoelectric structure. The colors of the ellipses express the β skew
 172 angle, which is a measure of asymmetry produced by 3-D structures.

173 Once the dimensionality was determined we applied the Groom and Bailey (GB) decomposition
 174 method (Groom & Bailey, 2002) following the multi-site, multi-frequency methodology of McNeice
 175 & Jones (2001), to correct MT data for distortion parameters. The low values of least square misfits
 176 between distortion model responses and the observed data (figures S1 and S2 in the electronic
 177 supplement), calculated at most periods of all sites, indicate that the proposed distortion model of

178 local 3D inhomogeneities superimposed on a regional 2D structure striking in an approximate
179 N45°W direction, appropriately resembles the MT dataset. Note that the results of this procedure
180 are the most accurate regional 2D impedances determined in a given coordinate system and are not
181 the same as those obtained by just rotating data into that coordinate system (the strategy used in
182 the previous modeling of this data set (Oskooi et al., 2016; Layegh-Haghighi et al., 2018)).

183 Distortion corrected TE and TM mode responses of regional structure recalculated by the GB
184 decomposition approach are then modeled throughout the regularized inversion algorithm
185 suggested by Rodi and Mackie (2001). The algorithm is implemented in the Geosystem's WinGLink
186 interpretation software and employs a non-linear conjugate gradient (NLCG) method to minimize a
187 penalty function composed of a least-square measure of data misfit and squared Laplacian of the
188 horizontal and vertical resistivity gradients representative of model roughness.

189 TM mode impedances expanding over six period band decades, between 0.0039- 1448 seconds,
190 have been considered for the inversion. However, in order to avoid intermediate-scale three-
191 dimensional effects that substantially can distort the TE mode responses (Ledo, 2005), their
192 maximum period was restricted to 10 s for the first 30 iterations and 100 s for the remaining.
193 Inaccurate data points with large error bars and those representing random scattering were
194 removed before the inversion. Furthermore, the D⁺ consistency assessment was performed where
195 essential and inconsistent data points were excluded from the inversion procedure.

196 Data errors have been used; otherwise, 10% and 5% ($\approx 1.45^\circ$ absolute) of the measured data were
197 set as the error values contaminated resistivities and phases, respectively.

198 Three-dimensional numerical experiments have shown that the TM mode impedances are more
199 robust to along strike structural changes (Ledo et al., 2002; Ledo, 2005; Wannamaker et al., 2009).
200 In addition, electric currents associated with the TM mode electromagnetic fields flow across
201 geoelectrical strike and enhance the resolution of large-scale conductive fault structure.
202 Accordingly, the TM mode impedances were emphasized through the model construction. The
203 inversion runs initiated from a homogeneous half space as the starting model, where the Persian
204 Gulf was the only feature fixed in order to model accurately the effects of the conductive sea water.
205 The error floors were 5% ($\approx 1.45^\circ$ absolute) for TM phases and 50% for TM resistivities. In the
206 following numerical experiments, the error floor of TM resistivities reduced to 10% and TE phases
207 and resistivities incorporated through the procedure, sequentially. The error floors of the final

208 inversion run were 5% for phases and 10% and 25% for TM and TE apparent resistivities,
209 respectively

210 Different data composition including TE, TM and bi-modal data were examined through inverse
211 modeling (results are presented in the supplementary material, figures S3 and S4). The fit of model
212 responses with the measured data are presented as the normalized data misfit for all stations along
213 the profile (figure S5) and pseudo sections of measured data and model responses in the
214 supplementary material (figures S6 and S7). While the RMS is less than 4 for the TE and TM modes,
215 but the TM mode responses provide a better fit with the measured data, in term of global RMS
216 misfit criterion (figure S5).

217 **4. Discussion**

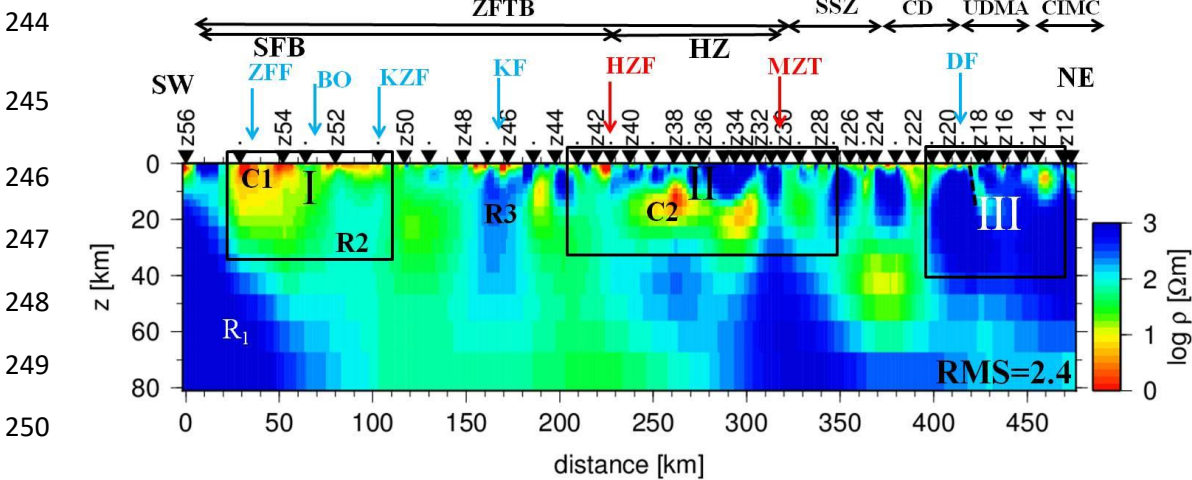
218 **4.1. Regional Geoelectric Structure**

219 The results of bi-modal MT data inversion (figure 3) will be argued in the following. The Arabian
220 crust is more conductive and heterogeneous than Eurasia. Fixing the Persian Gulf as a conductive
221 body in the starting model, a resistive structure (R1) is recovered beneath the southwest end of the
222 profile, resembling the downgoing Arabian plate. It was absent in the previous inversion results of
223 the data. To the southwest of the Kazerun fault, the resistivity model shows for the uppermost part
224 of the crust, a thick conductive layer (C1) from the surface to a depth of about 15 km, underlain by
225 the Pre-Cambrian crystalline basement of Arabia. Two resistive bodies (R₂, R₃) are imaged
226 coincident with the surface traces of right-lateral strike-slip faults: Kazerun and Karebas faults.
227 They are major basement faults which dragged and displaced anticline axes by at least 10 Km
228 (Khadiivi, 2011). A prominent conductive feature on the MT image appears at the crustal depths in
229 the middle part of the profile (C2), underneath the High Zagros. The surface trace of the MZT
230 coincides with the sharp conductivity contrast at the eastern edge of this feature. A thin near-
231 surface conductive layer, representing massive Neogene sediments of Central Iran is also imaged in
232 the upper crust, beneath the NE part of the profile.

233 The maximum smoothness constraint used in the MT inversion algorithm to find a unique inverse
234 model smears the conductor to unrealistically great depths. Furthermore, MT data are most
235 sensitive to the conductance (the product of the layer thickness and conductivity) of the subsurface
236 and different models with constant conductance but dissimilar thicknesses and conductivities can
237 fit equally well a given set of MT data. The solution is the constrained inversion where the bottom

238 of its starting model is fixed at a high value of 1000 Ωm . Then by moving upward the top of the
 239 resistive half-space until model responses could not fit the data properly, one could find the
 240 shallowest depth of the conductor's bottom, permitted by the data (Li et al., 2003). We applied this
 241 strategy and found that the conductive layer beneath the southwest of the profile is at least
 242 extended deeper than 10 km depth (figure S8, supplementary material).

243



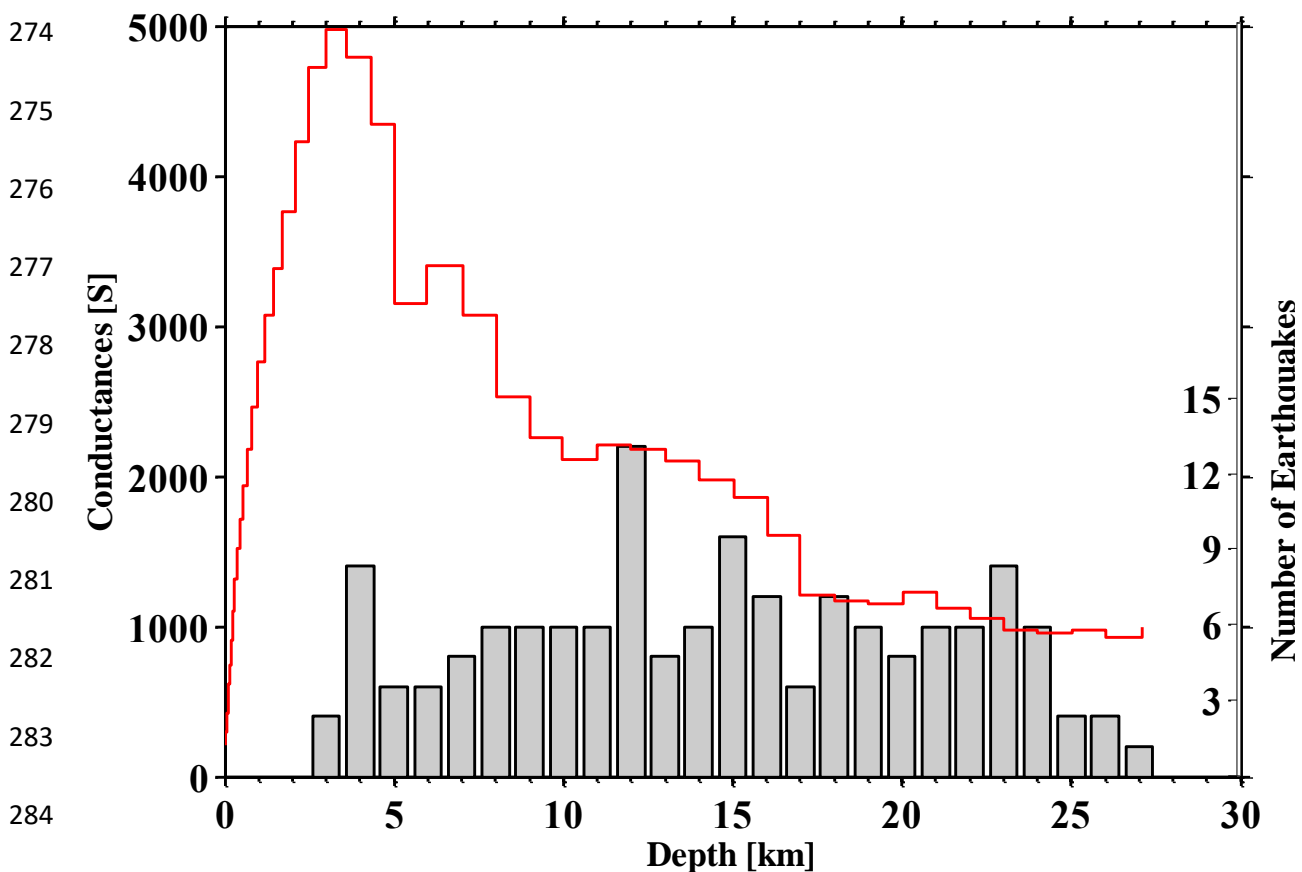
251 Figure 3. Non-linear 2-D inversion model of electrical resistivity beneath the Zagros profile obtained for
 252 joint TE and TM modes of the impedance tensor (a vertical exaggeration of 1.5:1 is used). Arabian plate
 253 below the SW of the profile is dipping NE ward, beneath Central Iran. Major faults are labeled as in figure 1
 254 (red: SW-NE striking faults, blue: N-S striking faults). Rectangles I, II, III represent spatial partitioning of
 the zones with high velocity/resistivity correlation outlined in figure 6 (zones I, II and III). Different grid
 sizes used in the seismic and MT models result in large coverage gaps.

255 Comparison with previous modeling results (Oskooi et al., 2013; Layegh-Haghighi et al., 2018)
 256 shows major conductive anomalies recovered at similar locations beneath the profile (figure S9 in
 257 the electronic supplement), but their spatial extent is much more restricted on the resistivity cross-
 258 section represented in figure 3, implying the fact that the MT data have been corrected for the twist
 259 and shear distortions prior to modeling. There are also some inconsistencies at regions where
 260 phase tensors show erratic behavior and large β skew angles.

261 **4.2. Origin of High Conductivity in Central Zagros**

262 A significant property of the model presented in figure 3 is the very high conductance (up to 6000 S,
 263 coincident with the conductance of a two-kilometer-thick layer composed of seawater) recovered
 264 in the upper crust with a generally decreasing trend from SW to the NE along with the profile

265 (figure S10 in supplementary material). The best explanation for such a high electrical conductance
 266 is saline fluids (reported in the eastern Zagros (Bosak et al., 1998)) filling the fractures and giving
 267 rise to the high electrical conductivity. Meteoric waters transported towards the fault zone by
 268 topography and/ or fluids circulating in the damage zone of a fault system characterize the upper
 269 few kilometers of the crust within a fault as a conductive zone, known as a fault zone conductor
 270 (FZC), (Ritter et al., 2005). The width and depth extent of the FZCs vary along the Zagros profile
 271 (e.g. confined conductive zones centered on the KF and HZF faults and weakly revealed
 272 conductivity at DF fault in figure 3). A distinct lack of FZC is observed beneath the MZT, implying
 273 that an FZC is not required to fit the data.



285 Figure 4. Conductance of the FZC related to ZFF as a function of depth (red line). It peaks
 286 between 2.5- 3 km depths. The histograms in gray show the distribution of earthquakes
 287 within 100 km of the MT profile. Note the spatial separation between depths of high fault
 zone conductance and high seismicity.

288 To further examine the potential role of fluids at the FZCs, we applied the method suggested by
 289 Bedrosian et al. (2004) to calculate the conductance (horizontally integrated conductivities) of
 290 these regions and compare it to the depth distribution of earthquakes associated with faults. We

291 integrated the conductance of cells restricted by the lateral boundaries of the conductive zones
292 centered on the major faults (with the high level of seismicity) in the SFB and compare it to the
293 depth distribution of earthquake hypocenters in this region. Figure 4 shows the result for the FZC
294 close to the ZFF (the results for the FZCs associated to the KZ and KB faults are presented as figures
295 S11 and S12 in the electronic supplement). The conductance peaks at 5000 S throughout the FZC of
296 ZFF and can be compared with that around KB fault. In all FZCs the conductance is greatest
297 between depths of 2.5 and 3.0 km. An outstanding feature in figure 4 is the spatial separation
298 between the depths of the peak FZC conductance and high seismicity. Seismicity begins at the depth
299 where the conductance decreases with increasing depth. The preferred explanation for this
300 scenario is the aqueous fluids for the enhanced conductivities of the FZCs around the faults. Fluid
301 rich regions are usually devoid of seismicity since shear stresses associated with brittle failure
302 could not be maintained in these regions.

303 An almost concave conductor has also been recovered in the MT image beneath the High Zagros (C2
304 in figure 3). The surface trace of the MZT coincides with a sharp conductivity contrast at the eastern
305 edge of this feature. Aqueous fluids, metallic minerals, grain boundary graphite films and molten
306 rocks are different physical causes that can be suggested for the observed conductor. However it's
307 unlikely that mineralization is responsible for C2 conductor, since such a large mineral deposit
308 would be expected to produce detectable magnetic and gravity anomalies that are not observed
309 (Abedi et. al., 2018). Furthermore, graphite films could not remain connected in crystalline
310 basement rocks documented for Zagros (Hatzfeld et al., 2003; Talebian and Jackson, 2004) and
311 cause an effective conductor. There is also no geological or geophysical evidence for molten rocks in
312 mid-crustal depths of High Zagros. There is no volcanic fields in this region and Plio-Quaternary
313 volcanism is widespread across eastern and central part of Iran close to the zones of presently
314 active faulting, for instance Dasht e Lut desert and Makran mountains (Walker et al., 2009). Fluids
315 generated from dehydration reactions within the subducting Arabian plate are the only candidate
316 that may be considered as the hydrological implication for the High Zagros conductor. This
317 assumption entails the saline fluids at hydrostatic pressures filling the interconnected fractures of
318 the crystalline basement, which inhibit the seismicity in this region. The distinct lack of FZC
319 corresponding to the MZT implies an impermeable fault seal preventing the cross fault fluid flow
320 transport or a very narrow FZC that cannot be resolved by MT.

321 **4.3 Comparisons with seismic velocity and seismicity data**

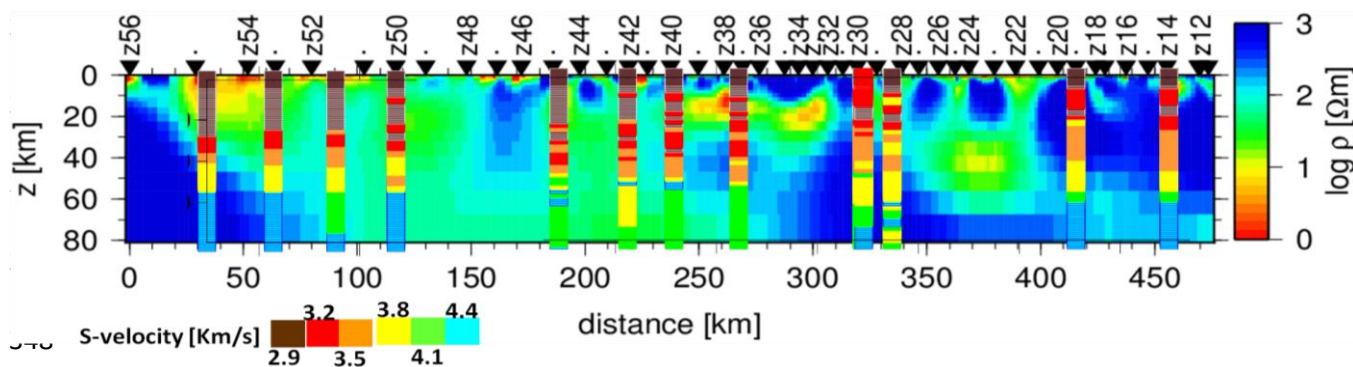
322 A reasonably comprehensive picture of the region is obtained by integrating seismic velocity model
323 and seismicity data with the final MT inversion model.

324 1D joint inversion of P-wave receiver functions and the surface wave dispersion data at
325 seismological stations along the same profile were juxtaposed to obtain a 2D S-velocity model
326 whose lateral variability was constrained by the Bouguer gravity anomaly data (Motaghi et. al.,
327 2015).

328 A qualitative comparison between the velocity and resistivity models is presented in figure 5.
329 Through this integrated interpretation approach, the limitations in sensitivity and resolution of
330 independent geophysical datasets as well as different numerical strategies used to invert these data
331 have to be considered. MT data were inverted using a 2D approach consisted of a minimum
332 smoothness constraint to regularize the inverse problem. However, 2D S-velocity model with more
333 continuous low and high-velocity domains (figure 6 in Motaghi et. al., 2015) was obtained by
334 combining 1D absolute S-velocity models of individual stations and smoothing the result with a
335 Gaussian filter width of 30 Km.

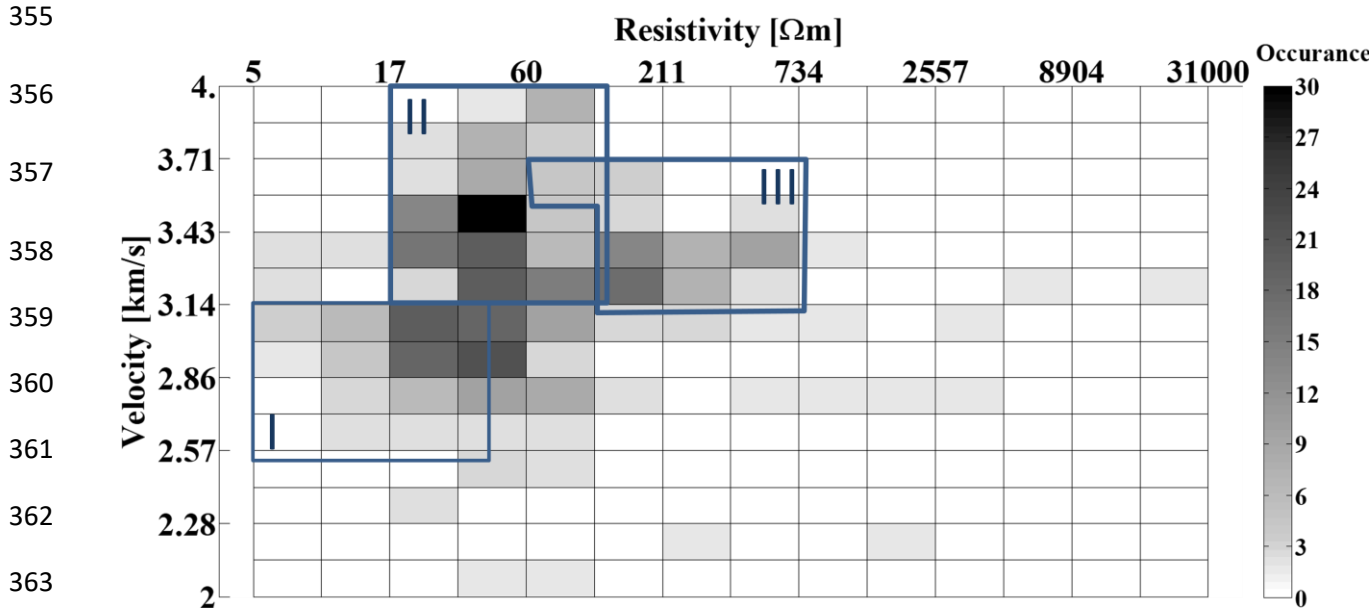
336 In general, it seems that domains of low velocities and resistivities beneath the south west of
337 Zagros, are spatially coincident which is consistent with the known geology of the region where an
338 upper layer of at least 10 km thickness composed of Cambrian to Miocene sediments overlays the
339 crystalline basement and produces an almost negligible magnetic response (Abedi et al., 2018)

340 Sparse lateral sampling of MT data (caused by large average site spacing of 15 km) as well as
341 smoothest 2D inversion modeling approach cause the upper crustal conductive layer (C1) to be
342 recovered discontinuous, beneath the SW of the profile. However, coincident seismic studies based
343 on juxtaposed 1D velocity models imaged more homogenous velocity structure in this region.



349 Figure 5. Electrical resistivity section overlain by S- wave velocity model from Motaghi et al. (2015).

350 We interpolate the coincident and independently derived seismic velocity (Motaghi et al., 2015)
 351 and electrical resistivity (figure 3) models on to a common grid to obtain a histogram of the
 352 correlation between V_s and electrical resistivity in the upper 28.5 km of the Zagros profile. A
 353 general increase of electrical resistivity with increasing seismic velocity, representative of
 354 decreasing porosity, is apparent (figure 6).



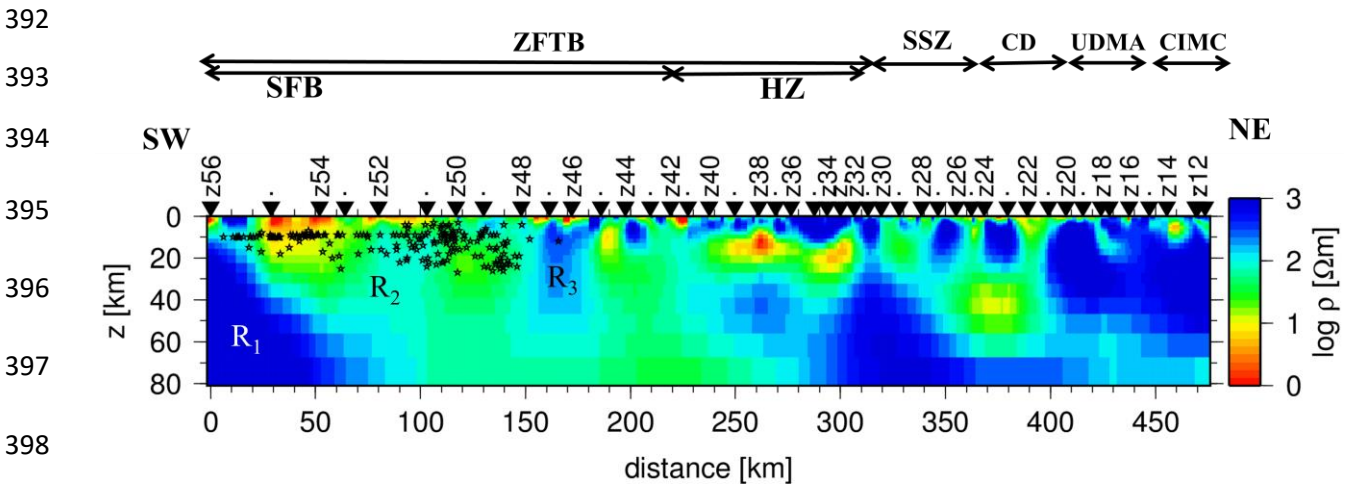
364 Figure 6. Quantitative correlation between resistivity and velocity models. A general increasing trend (dashed
 365 line) of velocity versus resistivity is apparent in this histogram. Also, three labeled zones of high correlation
 366 are presented in this figure.

366 Since the histogram grid is very coarse (of 1000 m, limited by the size of seismic model grid), only
 367 three localized zones (I, II and III in figure 6) have been chosen. The zones were mapped back into
 368 the resistivity section to determine the spatial regions where these zones derive (zones I, II and III
 369 in figure 3). The region of high resistivity/velocity (zone III) corresponds to the upper crust of
 370 central Iran Continental block. The zone (II) is defined by moderate resistivities and moderate to
 371 high velocities and is located beneath the High Zagros and SSZ. The zone (I) has the lowest
 372 resistivity/velocity values and coincides with the sedimentary cover of the Arabian crust.

373 The prominent conductivity contrast beneath the MZT corresponds to steep gradient in both
 374 Bouguer gravity and magnetic intensity (Abedi et al., 2018) as well as sharp boundary between low
 375 velocities of the ZFTB upper crust and higher velocities beneath SSZ and UDMA (figure 5). These
 376 concurrent changes in different physical properties provide strong support for a deep seated fault,
 377 cross-cutting the whole crust and upper mantle, as estimated by joint interpretation of seismic and

378 gravity data (Motaghi et. al., 2015). Although the authors show that a high velocity/density
 379 lithosphere beneath Zagros ($V_s \sim 4.8$ km/s, $\rho \geq 3.4$), representative of the leading edge of Arabian
 380 shield, is sinking beneath SSZ, UDMA and Central Iran, but this is not confirmed by our resistivity
 381 model. Long period MT measurements being able to penetrate deeper levels up to the lithosphere-
 382 asthenosphere boundary will be required to constrain more accurately the deep structure beneath
 383 Zagros suture zone.

384 Figure 7 shows pattern of crustal seismicity occurred within 100 km distance from the MT profile
 385 (white dots in figure 1) superposed on electrical resistivity section. Earthquake hypocenters are
 386 from an updated catalogue of 2500 earthquakes (red and white dots in figure 1) whose source
 387 parameters have been determined from locally and teleseismically recorded earthquakes
 388 (Karasozen et al., 2019). The authors used a calibrated earthquake relocation method improved by
 389 InSAR data. These seismic hypocentral calibrated locations of earthquakes (referred to as the
 390 Global Catalog of Calibrated Earthquake Locations (GCCEL)) are uploaded to the GCCEL catalog
 391 (<https://www.sciencebase.gov/catalog/item/59fb91fde4b0531197b16ac7>).



399 Figure 7. Seismicity data (black stars) provided by Karasozen et al. (2019) for 100 km strip on either
 400 sides of the MT transect (whose epicenters are plotted by the white dots in the figure1) are superposed
 on the electrical resistivity section.

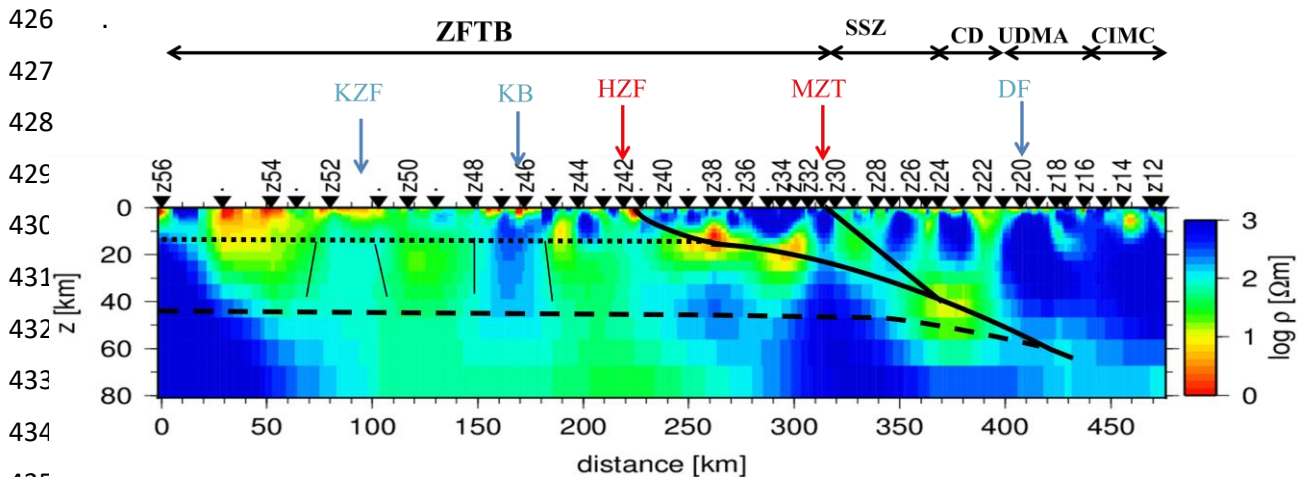
401 Towards northeast of the resistive structure recovered beneath the KB fault (R_3), the Zagros
 402 mountain belt is nearly devoid of seismicity. Seismicity in Zagros is most pronounced in the SFB.
 403 Despite high seismic activity in Zagros belt, no event has been located beneath the MZT region in
 404 central Zagros as well as in the SSZ (Paul et al., 2006).

405 The High Zagros includes NW-striking thrust and reverse faults with notable surface exposure
 406 where the most important ones are the MZT and HZF. However several seismogenic basement
 407 thrust faults, without surface rupturing are accommodated beneath the SFB. The main front fault
 408 (MFF) and the Zagros Foredeep fault (ZFF) are the two major thrusts in this region. Furthermore, a
 409 series of strike slip faults, striking roughly to the N-S direction (KZ, BO, KB, SP and SV faults) are the
 410 only major faults scratching the earth surface in this region (Figure 1).

411 Thrust faulting is the most frequent earthquake mechanism that usually takes place in the Zagros.
 412 The earthquakes mainly occur within the lower parts of the SFB sedimentary cover rather than the
 413 HZ (figure 7) and are restricted to low elevated regions with an average strike direction along NW-
 414 SE azimuth, coincident with the range orientation. They are very rare and usually absent beneath
 415 HZ and farther to the north east in the CIMC (figure 1). Weak horizons located at the base (the
 416 Hormoz evaporate), in the middle and upper parts (e. g. Gurpi Marls, Gachsaran evaporates) of the
 417 cover form a regional barrier to vertical rupture propagation and cause moderate size earthquakes
 418 with magnitudes $M_w \leq 6.1$ to be the typical seismicity of the SFB (Nissen et al., 2011).

419 The intense deformation within the ZFTB spans brittle damage elements (minor faults and slip-
 420 surface with or without striation) around different faults in this region and maintains a connected
 421 network for fluids released into the FZCs. Dehydration reactions within the subducting Arabian
 422 plate (in continental crust, mostly due to the amphibolites to granulites metamorphism (Glover and
 423 Vine, 1995)), provide a continuous recharge of fluids (Bedrosian, 2007).

424 Dashed and dotted lines in figure 8 represent respectively the Moho discontinuity and the
 425 detachment level of the folded sedimentary cover.



435 Figure 8. Geological interpretation of the MT model (see explanation on the text). The main faults cross-cutting the
 436 profile, are indicated by the arrows (in red with mainly SW-NE strike and in blue mainly N-S strike). The dotted line
 437 indicates the detachment level of folded sedimentary cover (10 – 15 km thick), corresponding to the Hormuz salt
 formation. The dashed line indicates Moho, inferred from seismic studies (Paul et al. 2010).

438
439 The Moho depth is inferred from seismic studies (Paul et al. 2010). The detachment level of folded
440 sedimentary corresponds to the Hormuz salt formation. Both, the salt formation and the
441 sedimentary cover on top are imaged as low resistivity structures in the model (between sites z56
442 and z42) with values lower than 60-70 Ωm .

443 This detachment level joins the trace of the HZF at depth (black continuous dipping line in figure 8).
444 The HZF allows thrusting the sedimentary cover and uploading the older and more resistive rocks
445 (Paleozoic rocks), between sites z42 and z32, with resistivity values more than 500 Ωm . The
446 Arabian crust, between the detachment level and the Moho, contains heterogeneous blocks (as
447 Kazerun Fault (KZF)) probably inherited from Precambrian times. They are imaged as zones of low
448 and high resistivities (marked by short vertical black lines in figure 8). The earthquakes are
449 concentrated in a specific seismic zone extended at the basement depths between sites z54 and z46
450 (see figure 7). By contrast, the seismicity is scarce to the NE of the site z45. To explain this feature
451 the resistive structure beneath Karehbas fault, KB, (sites z47-z46) could be considered as a low
452 permeable zone, retaining the fluids released along with the HZF and leading to a more ductile
453 behavior of the crust located to the NE of the KB fault.

454 Finally, the second black continuous dipping line (in figure 8) from MZT represents the contact
455 between Arabian and Iranian plates. On the side of the Iranian plate, the section shows lateral
456 changes in resistivity structure that can be associated to heterogeneous blocks of conductive
457 metamorphic materials beneath the SSZ and the resistive volcanic blocks of oceanic crust
458 (ophiolites) beneath the UDMA.

459
460 **Conclusion**

461 An integrated geophysical interpretation along a profile across central Zagros is proposed based
462 upon distortion corrected MT data as well as seismic velocity and seismicity data. Galvanic
463 distortion analysis performed on MT data results the most accurate 2D impedances in regional
464 coordinate system. The strategy used to reduce 3D effects from 2D inversion of these data,
465 produces a robust geoelectric model whose main features are compatible with the geology and
466 tectonics of this region. Within the SFB of Zagros folded belt to the South west of the KZF, the upper
467 crust is characterized by a zone of low resistivity and velocity extending from surface to depths
468 more than 10 km. This feature is attributed to the thick sedimentary sequence of the Arabian
469 platform. A quantitative correlation between resistivity and velocity models shows a general

470 increasing trend of velocity versus resistivity. Furthermore, three regions of high correlation were
471 determined.

472 Close to the faults, the possible effects of fluid filled voids and fractures within brecciated and
473 damaged zones of the faults have also been considered. An investigation of the conductance around
474 the major faults in this region shows its decreasing trend with increasing depth. The combination of
475 seismicity data with the conductance values at the FZCs suggests aqueous fluids for the enhanced
476 conductivities. It should be noted that the inferred fluids related to the FZCs is best resolved to be
477 far from the source region of the earthquakes. Thus we propose a scenario for the fluid distribution
478 beneath central Zagros controlling its seismic behavior. However, additional geophysical data
479 including 3D studies of the major faults is essential to further understand the tectonic processes at
480 the Zagros collision belt.

481

482 **References**

483 **Abedi, M., Fournier, D., Devriese, S., Oldenburg, D. W., 2017.** Potential field signatures along the
484 Zagros collision zone in Iran. *Tecto*, doi:10.1016/j.tecto.2017.10.012.

485 **Agard, P., Omrani, J., Jolivet, L., Whitechurch, H., Vrielynck, B., Spakman, W., Monié, P., Meyer, B.,**
486 **Wortel, R., 2011.** Zagros orogeny: a subduction-dominated process. *Geol. Mag.*
487 <https://doi.org/10.1017/S001675681100046X>.

488 **Ague J, Park J, Rye DM (1998)** Regional metamorphic dehydration and seismic hazard. *Geophys Res*
489 *Lett* 25:4221–4224

490 **Bedrosian, P., Unsworth M, Egbert G, Thurber C (2004)** Geophysical images of the creeping San
491 Andreas Fault: implications for the role of crustal fluids in the earthquake process. *Tectonophysics*
492 358, doi:10.1016/j.tecto.2004.02.010.

493 **Bedrosian, P.A., (2007),** MT+, Integrating magnetotellurics to determine earth structure, physical
494 state, and processes, *Surv. Geophys.*, 28, 121–167.

495 **Bosak, P., Jaros, J., Spudil, J., Petr Sulovsky, P. &Vaclavek, V., 1998.** Salt Plugs in the Eastern Zagros,
496 Iran: results of regional geological reconnaissance, *Geoline*, **7**, 174.

497 **Caldwell, T. G., H. M. Bibby, and C. Brown (2004),** Themagnetotelluric phase tensor, *Geophys. J. Int.*,
498 158, 457–469.

499 **Chave, A. D., and A. G. Jones (2012),** *TheMagnetotelluric Method—Theory and Practice*, 570 pp.,
500 Cambridge Univ. Press, Cambridge, U. K.

501 **Dehghani**, G.A., Makris, J., 1984. The gravity field and crustal structure of Iran, N. Jb. Geol. Palaeont.
502 Abh., **168**, 215–229.

503 **Gabàs**, A., Macau, A., Benjumea, B. et al., 2016. Joint Audio-Magnetotelluric and Passive Seismic
504 Imaging of the Cerdanya Basin Surv Geophys (2016) 37: 897. [https://doi.org/10.1007/s10712-](https://doi.org/10.1007/s10712-016-9372-4)
505 016-9372-4.

506 **García-Yeguas**, J. Ledo, P. Piña- Varas, J. Prudencio, P. Queralt, A. Marcuello, J.M. Ibañez, B. Benjumea,
507 A. Sánchez-Alzola, N. Pérez. A 3d joint interpretation of magnetotelluric and seismic tomographic
508 models: the case of the volcanic island of Tenerife Comput. Geosci., 109 (2017), pp. 95-105.

509 **Hatzfeld**, D., Tatar, M., Priestley, K., Ghafory-Ashtyany, M., 2003. Seismological constraints on the
510 crustal structure beneath the Zagros mountain belt (Iran), *Geophys. J. Int.*, **155**, 403–410.

511 **Karasözen**, E., Nissen, E., Bergman, E. A., and Ghods, A. (2019). Seismotectonics of the Zagros (Iran)
512 From Orogen-Wide, Calibrated Earthquake Relocations. Journal of Geophysical Research: Solid
513 Earth, <https://doi.org/10.1029/2019JB017336>.

514 **Khadivi**, S., Tectonic evolution and growth of the Zagros Mountain Belt (Fars, Iran): constraints
515 from magnetostratigraphy, sedimentology and low- temperature thermo chronometry, Institut des
516 Sciences de la Terre de Paris.

517 **Layegh**, T., Montahaei, M and Oskooi, B. (2018) MT data inversion and sensitivity analysis to image
518 electrical structure of Zagros collision zone. Journal of Applied Geophysics. 148, 23-32

519 **Ledo**, J., 2005, 2-D versus 3-D magnetotelluric data interpretation. Surveys in Geophysics, 26(5),
520 511–543. <https://doi.org/10.1007/s10712-005-1757-8>.

521 **Ledo**, J., Queralt, P., Martí, A., & Jones, A. G. (2002). Two-dimensional interpretation of three-
522 dimensional magnetotelluric data: An example of limitations and resolution. Geophysical Journal
523 International, 150(1). <https://doi.org/10.1046/j.1365-246X.2002.01705.x>

524 **Manaman**, N.S., Shomali, H., Koyi, H., 2011. New constraints on upper-mantle S-velocity structure
525 and crustal thickness of the Iranian plateau using partitioned waveform inversion. Geophys. J. Int.
526 184 (1), 247–267.

527 **Masson**, F., Chéry, J., Hatzfeld, D., Martinod, J., Vernant, P., Tavakoli, F., Ghafory-Ashtiani, M., 2005.
528 Seismic versus aseismic deformation in Iran inferred from earthquakes and geodetic data. Geophys.
529 J. Int. 160, 217–226.

530 **McNeice**, G.W., Jones, A.G., 2001. Multisite, multifrequency tensor decomposition of magnetotelluric
531 data. *Geophysics* 66, 158–173.

532 **Molinario**, M., Leturmy, P., Guezou, J.-C., Frizon de Lamotte, D.&Eshraghi, S.A., 2005. The structure
533 and kinematics of the southeastern Zagros foldthrust belt, Iran: from thin-skinned to thick-skinned
534 tectonics, *Tectonics*, **24**, TC3007, doi:10.1029/2004TC001633.

535 **Motaghi**, K., Tatar, M., Priestley, K., Romanelli, F., Doglioni, C., Panza, G.F., 2015. The deep structure
536 of the Iranian Plateau. *Gondwana Res.* 28 (1), 407–418.

537 **Motaghi**,K,Shabanian E, Tatar M, Cuffaro M, Doglioni C, 2017,The south Zagros suture zone in
538 teleseismic images.*Tectonophysics* 694, 292-301.

539 **Mouthereau**, F., 2011. Timing of uplift in the Zagros belt/Iranian plateau and accommodation of late
540 Cenozoic Arabia–Eurasia convergence. *Geol. Mag.* 148 (5–6), 726–738.

541 **Nissen**, E., Tatar, M., Jackson, J. A. and Allen M. B. (2011), New views on earthquake faulting in the
542 Zagros fold-and-thrust belt of Iran, *Geophys. J. Int.*, 186, 928–944.

543 **Ogawa** Y, Mishina M, Goto T, Satoh H, Oshiman N, Kasaya T, Takahashi Y, Nishitani T, Sakanaka S,
544 Uyeshima M, Takahashi Y, Honkura Y, Matsushima M (2001) Magnetotelluric imaging of fluids
545 inintraplate earthquakes zones, NE Japan back arc. *Geophys Res Lett* 28:3741–3744.

546 **Oskooi**, B., Pedersen, L.B., Koyi, H.A., 2013. Magnetotelluric signature for the Zagros collision.
547 *Geophys. J.* 196 (3), 1299–1310 International Volume. (DOI: 10.1093/gji/ggt 466).

548 **Paul**, A., Kaviani, A., Hatzfeld, D., Vergne, J., Mokhtari, M., 2006. Seismological evidence for crustal-
549 scale thrusting in the Zagros mountain belt (Iran). *Geophys. J. Int.* 166, 227–237.

550 **Paul**, A., Kaviani, A., Hatzfeld, D., Tatar,M., Pequegnat, C., 2010. Seismic imaging of the lithospheric
551 structure of the Zagros mountain belt (Iran). In: Leturmy, P., Robin, C. (Eds.), *Tectonic and*
552 *Stratigraphic Evolution of Zagros and MakranDuring the Meso-CenozoicSpecial Publications* 330.
553 Geological Society, London, pp. 5–18.

554 **Pirouz**, M., Avouac, J-P, Hassanzadeh, Kirschvink, J. L., Bahroudi, A,; Early Neogene foreland of the
555 Zagros, implications for the initial closure of the Neo-Tethys and kinematics of crustal
556 shortening, *Earth and Planetary Science Letters*, 2017, <http://dx.doi.org/10.1016/j.epsl.2017.07.046>

557 **Rodi**, W., Mackie, R.L., 2001. Nonlinear conjugate gradients algorithm for 2-D magnetotelluric
558 inversions. *Geophysics* 66, 174–187.

559 **Snyder, D. B., Barazangi, M., 1986.** Deep crustal structure and flexure of the Arabian plate beneath
560 the Zagros collisional mountain belt as inferred from gravity observations, *Tectonics*, **5**, 361–373.

561 **Sherkati, S., Letouzey, J., Frizon de Lamotte, D., 2006.** Central Zagros fold-thrust belt (Iran): new
562 insights from seismic data, field observation, and sandbox modeling. *Tectonics* **25**, TC4007,
563 doi:10.1029/2004TC001766.

564 **Soleimani M., Jodeiri Shokri B., Rafiei Mehrnoush., 2017,** Improvement of seismic structural
565 interpretation of Zagros fold-thrust belt by dip scanning in common diffraction surface imaging
566 method. *Acta Geod Geophys*, **52**:283–299 DOI 10.1007/s40328-016-0182-4.

567 **Talebian, M. & Jackson, J., 2004,** A reappraisal of earthquake focal mechanisms and active
568 shortening in the Zagros mountains of Iran, *Geophys. J. Int.*, **156**, 506–526.

569 **Unsworth, M.J., 2010.** Magnetotelluric studies of active continent-continent collisions. *Surv.*
570 *Geophys.* **31**, 137–161.

571 **Vernant, P., Nilforoushan, F., Hatzfeld, D., Abbassi, A. B., Vigny, C., Msson, F., Nankali, H., Martinod, J.,**
572 **Ashtiani, A., Bayer, R., Tavakoli, F., Chery, J., 2004.** Present day crustal deformation and plate
573 kinematics in the Middle East constrained by GPS measurements in Iran and northern Oman.
574 *Geophysical Journal International*, **157**, 381–398.

575 **Wannamaker, P. E., T. G. Caldwell, G. R. Jiracek, V. Maris, G. J. Hill, Y. Ogawa, H. M. Bibby, S. L. Bennie,**
576 **and W. Heise (2009),** Fluid and deformation regime of an advancing subduction system at
577 Marlborough, New Zealand, *Nature*, **460**, 733–736, doi:10.1038/nature08204.

578

1 Supporting Information for “Integrated interpretation of geophysical data
2 from Zagros mountain belt (Iran)”

3 Mansoure Montahei, Pilar Queralt, Juanjo Ledo, Behrooz Oskooi, Josep A. Muñoz, and Alex
4 Marcuello

5

6 **Contents:**

- 7 - Inversion result of the individual TE and TM modes impedances
8 - Individual RMS misfit for each site
9 - Pseudosections of measured data and model responses
10 - Constraint inversion Results
11 - Comparision between the newest inversion model and the previously
12 published ones
13 - The model conductance along the profile
14 - Comparision between depth distribution of earthquakes and the
15 conductance of the FZCs

16

17

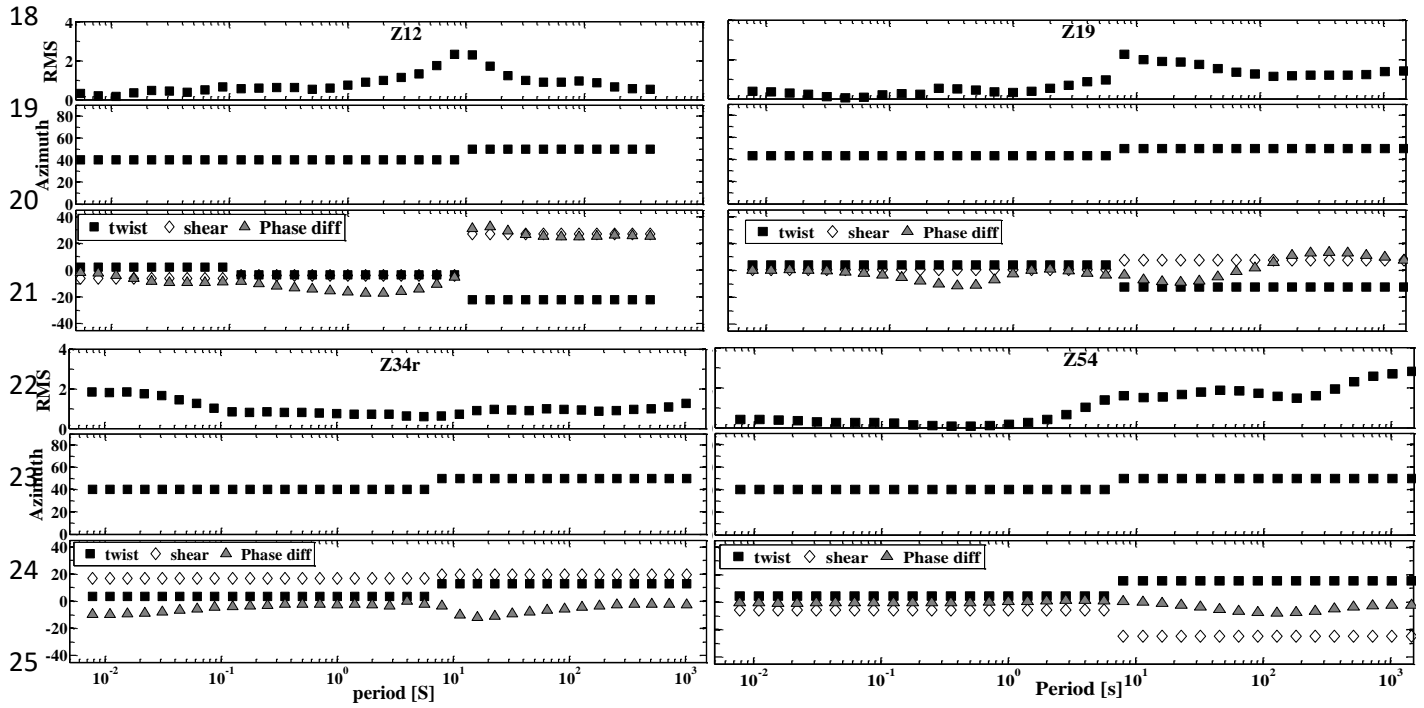


Figure S1. Decomposition results showing the RMS misfit, preferred strike direction and distortion parameters (shear and twist) for data constrained to three period bands at representative sites located at different geological units.

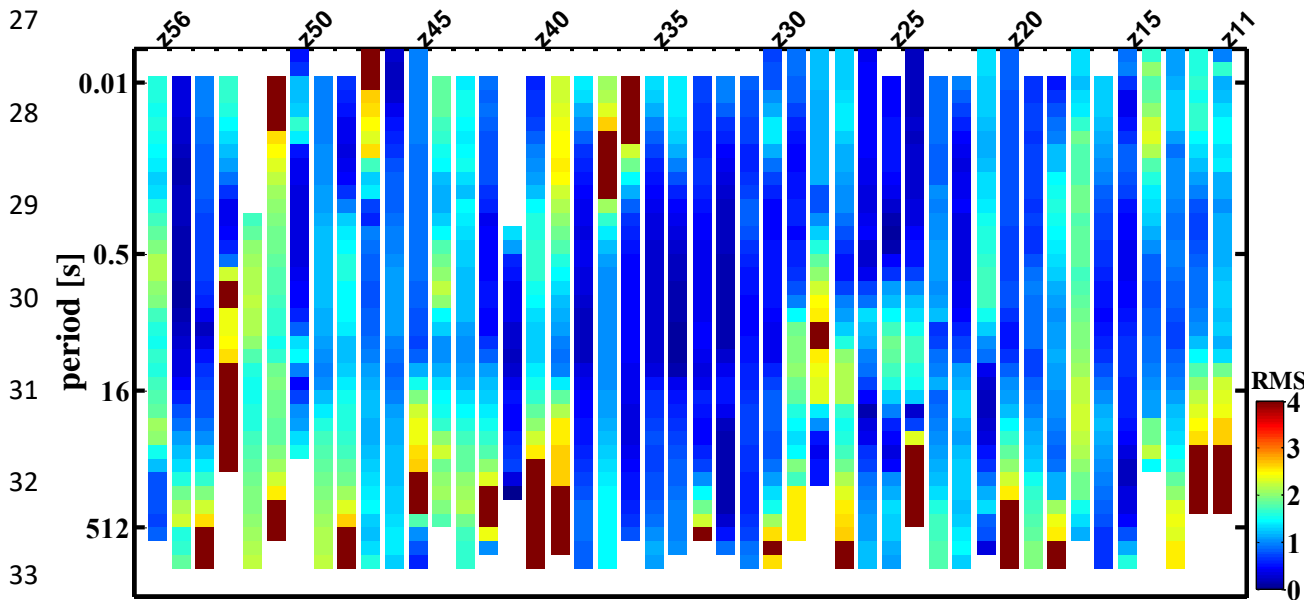


Figure S2. Data misfit values calculated from decomposition models for each site along the Zagros profile for the whole frequency range. MT responses were recalculated for the regional strike direction fixed at -45° .

35

36

37

38

39

40

41

42

43

44

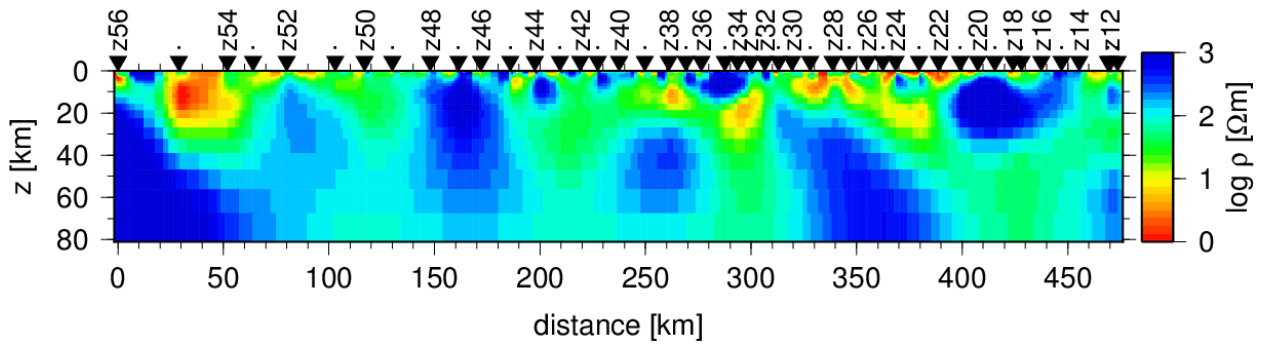
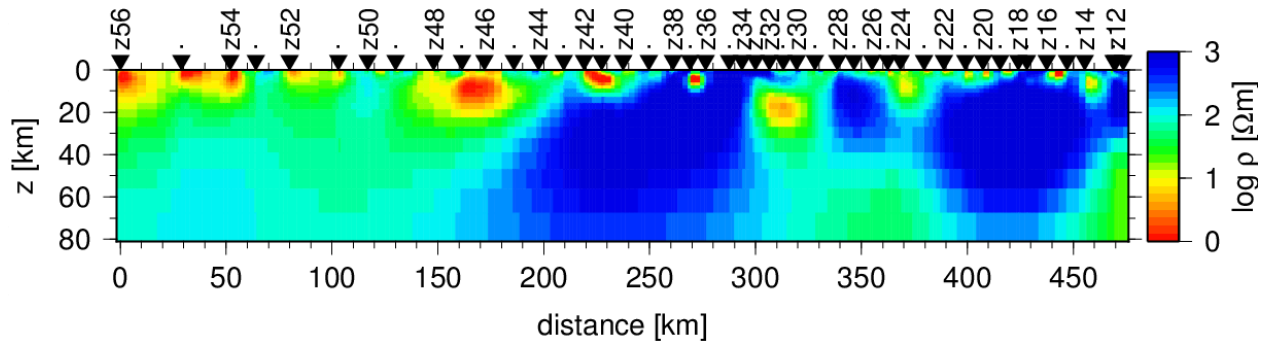


Figure S3. Inversion result of the TM mode impedances

44

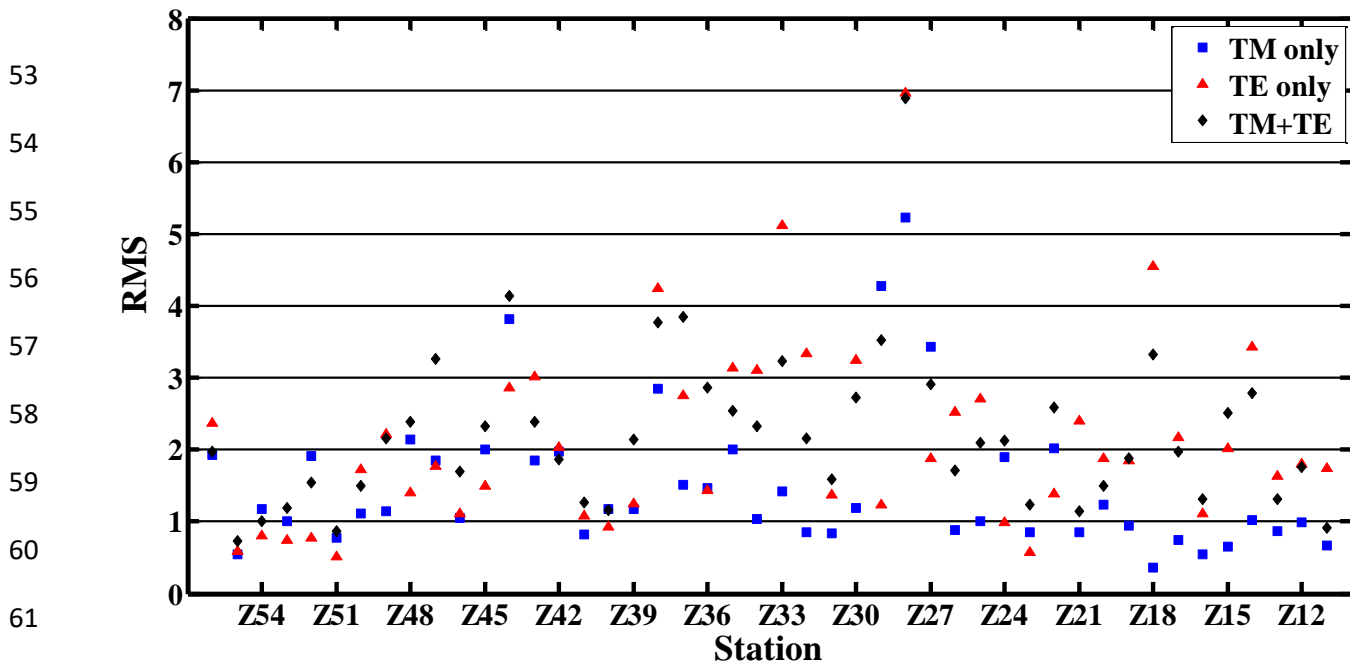


50

Figure S4. Inversion result of the TE mode impedances

51

52



62 Figure S5. Individual RMS site misfits for the final two-dimensional resistivity models along the
 63 Zagros MT profile, shown in Figure 3.

64

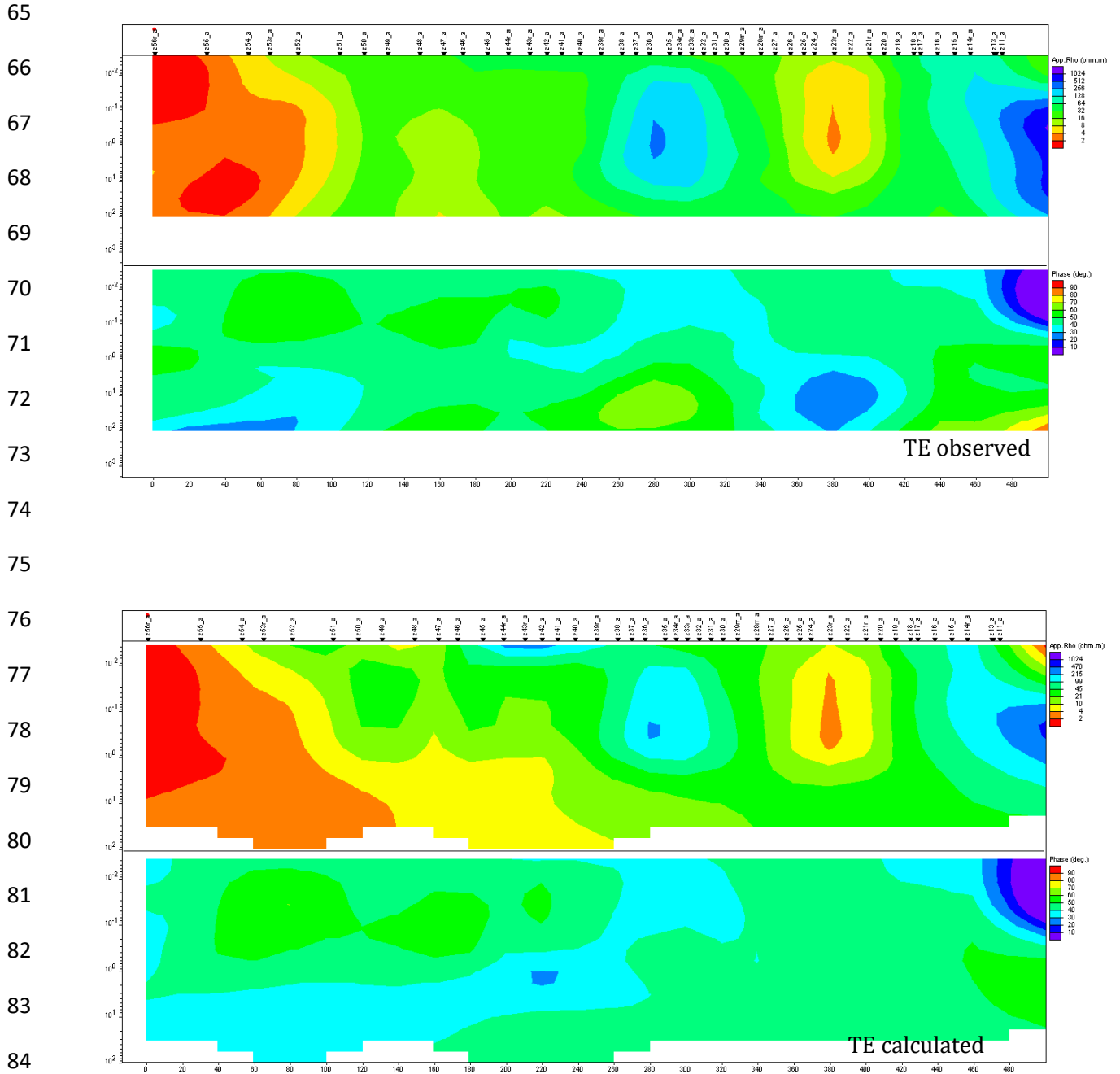


Figure S6. Pseudosection of the measured and calculated TE mode data

90

91

92

93

94

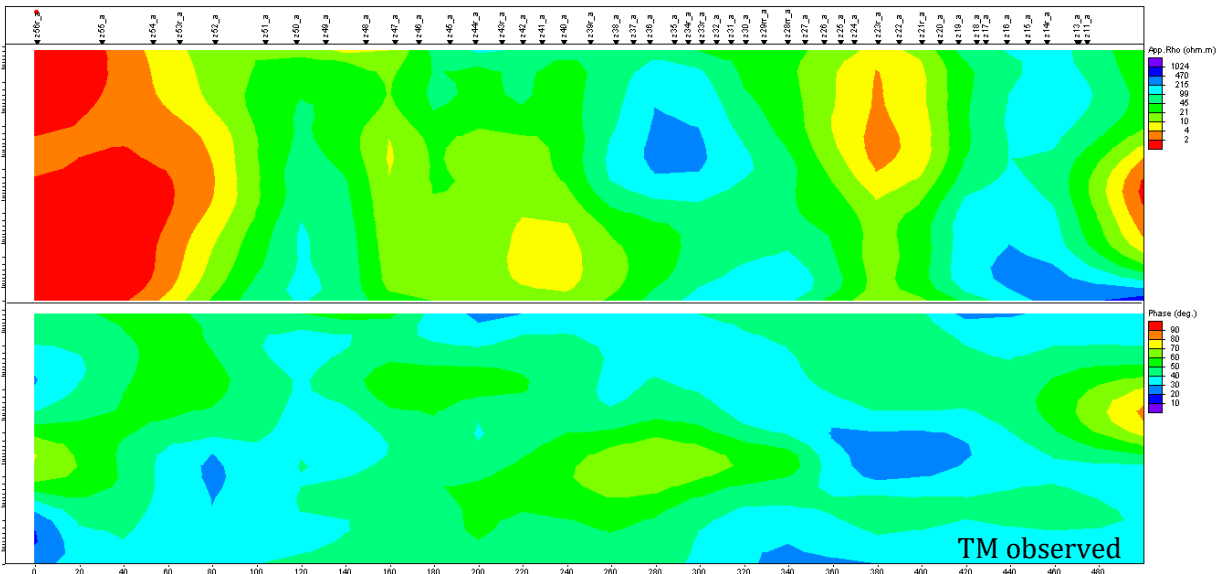
95

96

97

98

99



100

101

102

103

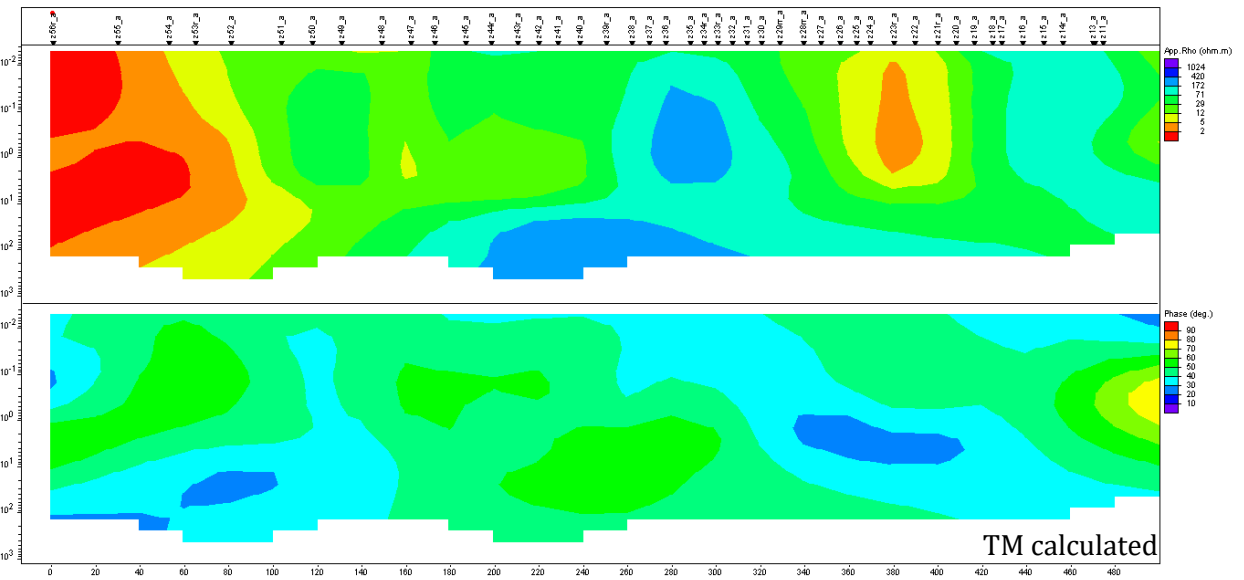
104

105

106

107

108



109

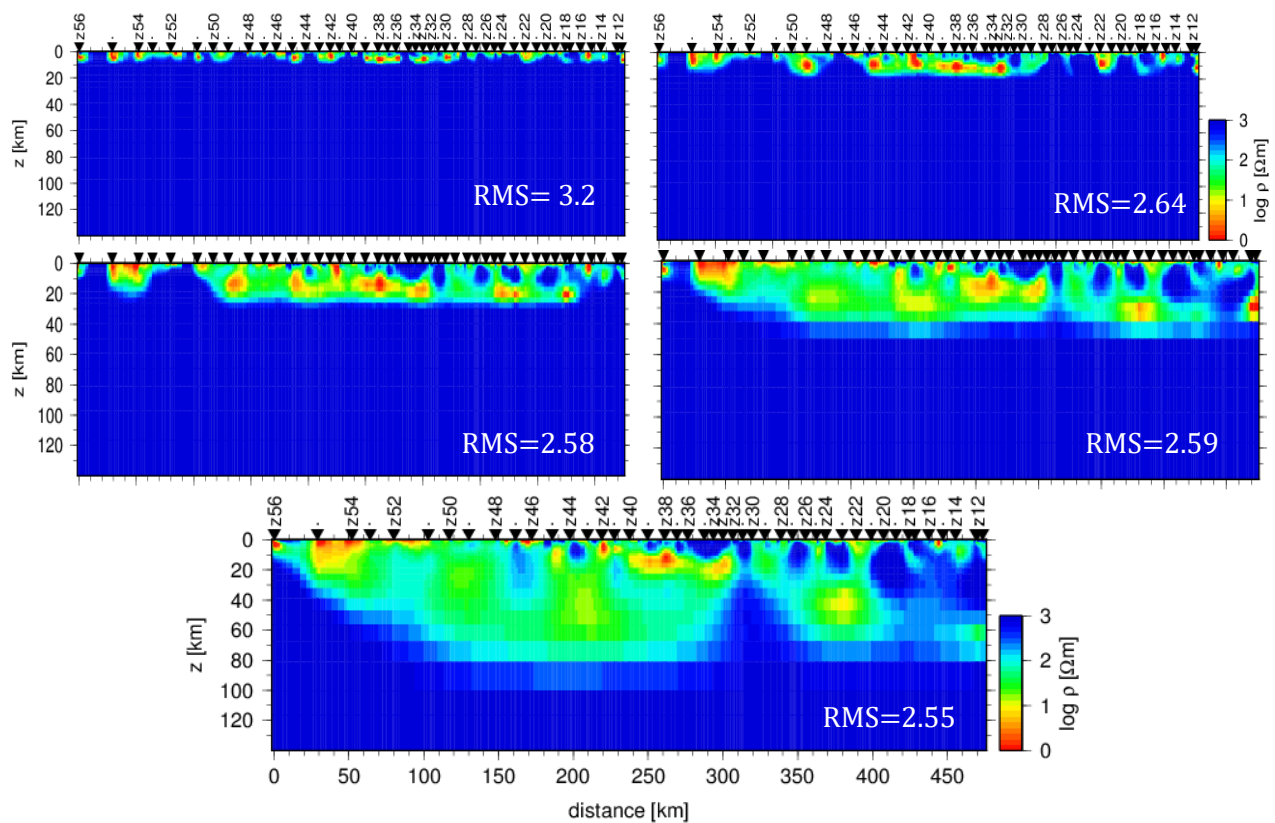
110

Figure S7. Pseudosection of the measured and calculated TM mode data

111

112 MT data could constrain the conductance and the depth to the top of a conductive layer and
 113 they are insensitive to the bottom of a conductor (Bedrosian, 2007). Therefore, the data
 114 misfit would not be affected by replacing a resistive half space in the bottom of the model.
 115 Moving upward the top of the resistive half space until model responses could not fit the
 116 data properly, one could find the shallowest depth of the conductor bottom, permitted by
 117 the data (Li et al., 2003). we fixed the bottom of the resistivity starting model, beneath 100
 118 Km depth with a 1000 Ωm half space and move its top upward to the 50, 40, 30, 20 and 10
 119 Km, sequentially. The results of this process are presented in the following figures;

120 It appears that the conductive layer beneath the south west of the profile is at least
 121 extended deeper than 10 km depth.



122 Figure S8. Constrained inversion results as the basement is moved up and the resistivity of half space
 123 remain fixed during the inversion. The achieved RMS is given for all models.

124

125

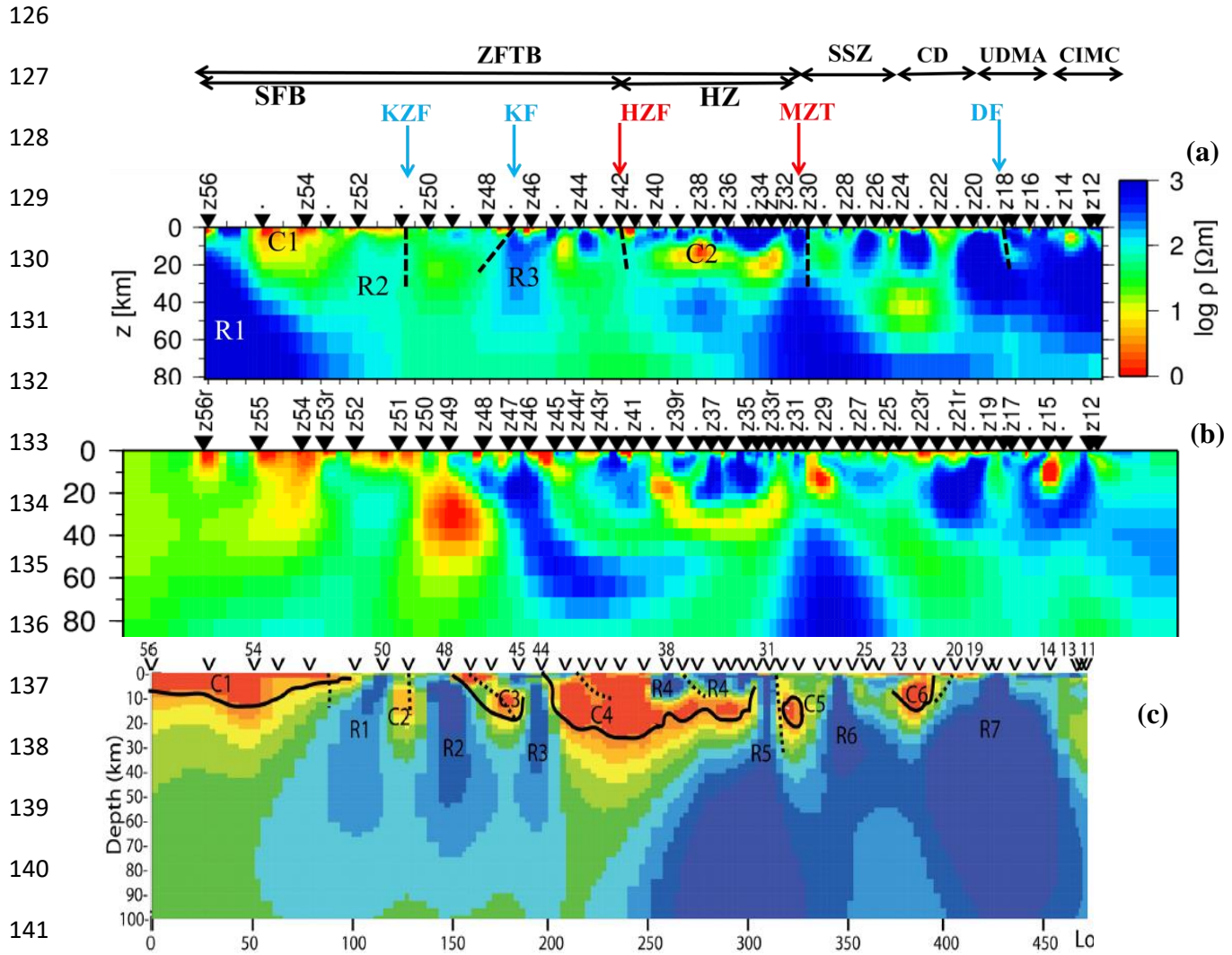


Figure S9. Inversion results obtained in (a) current study from distortion corrected MT data. (b) Layegh-Haghighi et al., 2018. (c) Oskooi et al., 2013.

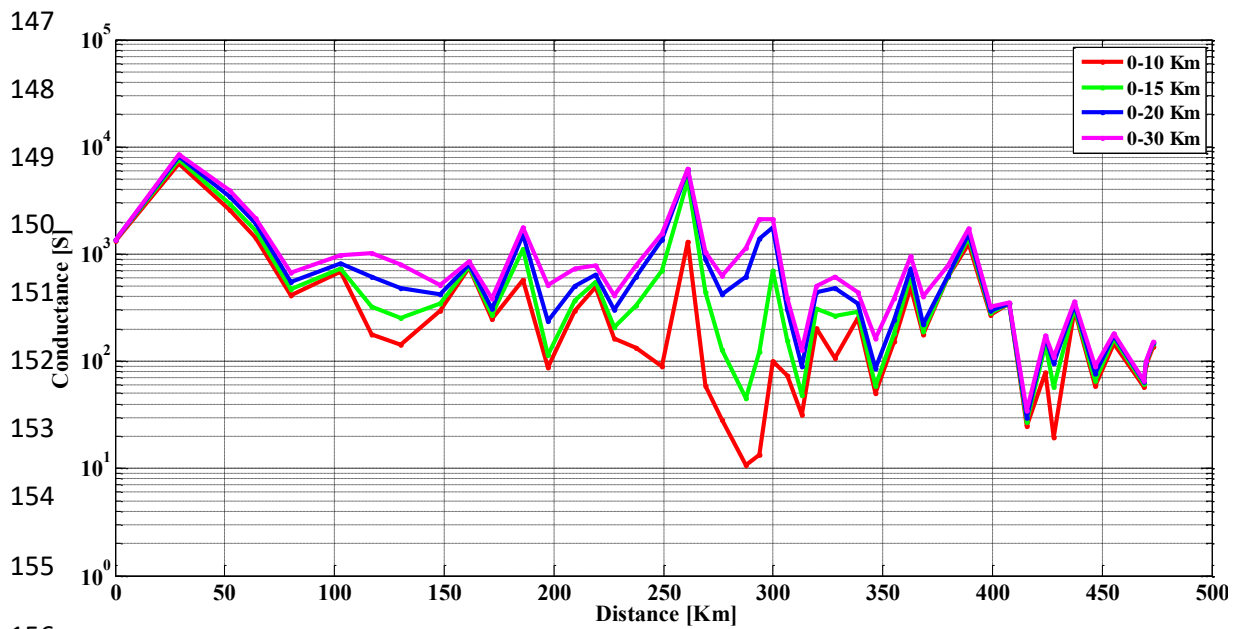


Figure S10. The model conductance for the Zagros profile, integrated from top to the depths of 10, 15, 20 and 30 km.

162
163
164
165
166
167
168
169
170
171
172
173
174
175
176
177
178

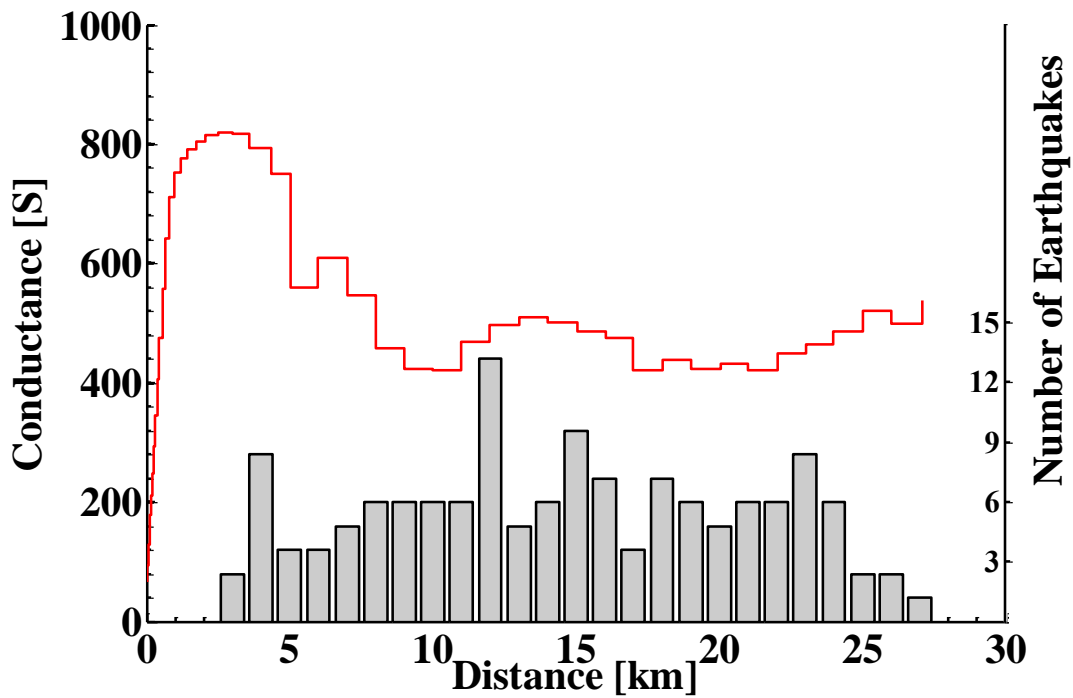


Figure S11. Conductance of the FZC related to KZ fault as a function of depth. It peaks between 2.5-3 km depths. The histograms in gray show the distribution of earthquakes within 100 km of the MT profile. Note the spatial separation between depths of high fault zone conductance and high seismicity

179
180
181
182
183
184
185
186
187
188
189
190
191
192
193
194

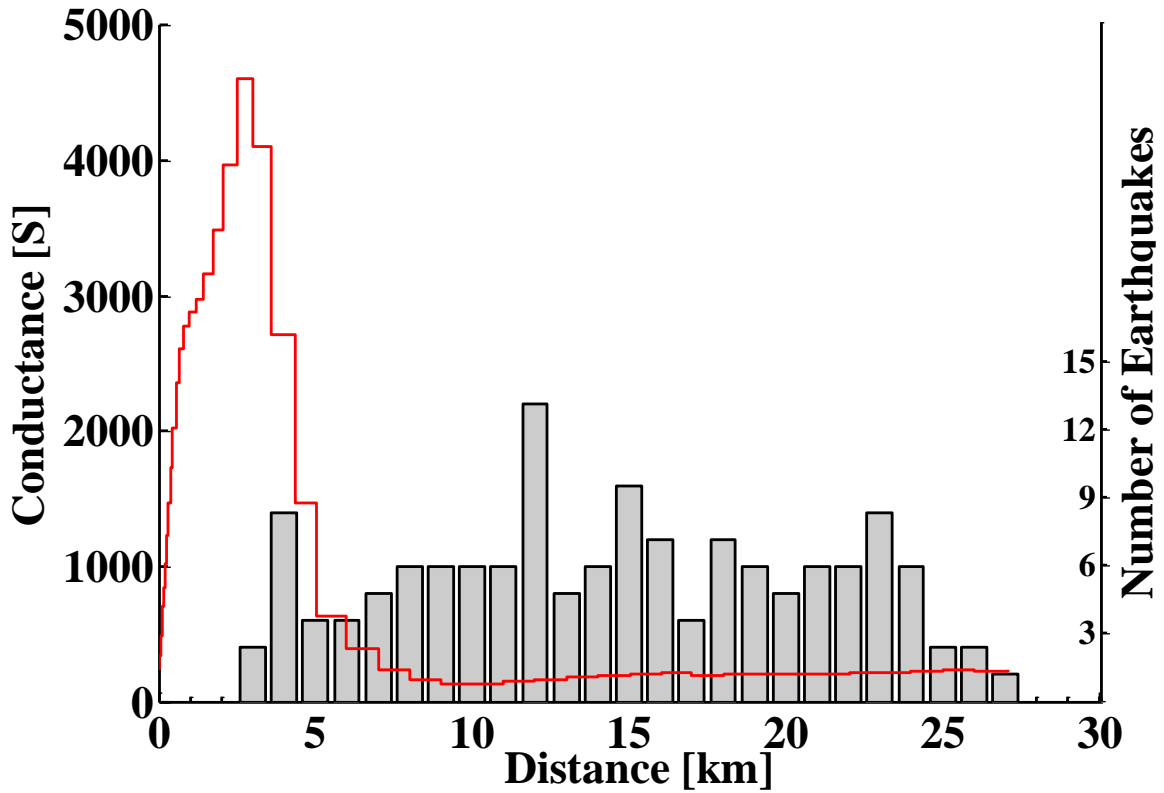


Figure S12 Conductance of the FZC related to KB fault as a function of depth. It peaks between 2.5-3 km depths. The histograms in gray show the distribution of earthquakes within 100 km of the MT profile. Note the spatial separation between depths of high fault zone conductance and high seismicity.